Fixed-pattern noise suppression in low-sensing environment of Time-of-flight devices

Mihail Georgiev, Robert Bregovic, Atanas Gotchev
Tampere University of Technology, Tampere, Finland
mihail.georgiev@tut.fi, robert.bregovic@tut.fi, atanas.gotchev@tut.fi

***Abstract*—In this paper, we emphasize the importance of fixed-pattern noise (FPN) that occurs in Time-of-Flight (ToF) devices that operate in the so-called low-sensing environment. We propose a method for designing FIR filters that can be used for suppressing the FPN. We illustrate by means of two experiments the importance of dealing with the FPN, before conventional denoising algorithms are applied.**

Keywords—FPN, Fixed-pattern-noise, Time-of-Flight, low-sensing environment, denoising

I. INTRODUCTION

In recent years there is a reviving interest in active range sensing devices based on the Time-of-flight (ToF) principle [1, 2, 3]. In such devices the range is estimated by measuring the time required for a light signal to illuminate a scene and "travel back" to the sensor. However, ToF devices still have low resolution (e.g. 204x204 pixels) and high power consumption [2]. The demand for low power is especially important when ToF sensors need to be integrated in power-constrained (e.g. mobile) devices. In the case the power of the light emitted by the ToF device is lowered, the device is said to be working in low-sensing mode. For such mode, high measurement errors are possible for objects (areas) of low reflectivity [3, 4, 5, 6] and a post-capture denoising is required. There is a relation between the measured amplitude, which quantifies the reflectivity of objects and the error in distance measurements [5, 6]. In situations when the ToF device is forced to work in low-sensing mode, the amplitude is quite low and the distance measurements are more erroneous. Still, the reflectivity information can be utilized for effective post-capture denoising [7, 8, 9, 10]. After it, the range data appears within the error limits as it was captured in normal-operating mode.

In our earlier works, we have observed that the performance of the denoising methods is quite much influenced by the presence of noise component, characterized as fixed-pattern noise (FPN), similarly to phenomena in other 2D imaging devices [5, 11, 12, 13]. Such noise component has to be suppressed by proper linear filtering before a more dedicated denoising algorithm can be efficiently applied.

In this paper, we analyze the influence of FPN on ToF data denoising in more detail. We quantify the performance of several modern denoising algorithms [14, 15, 16, 17, 18], specifically selected since they have been used in similar applications [7, 17, 19, 20, 21]. Our experiments show that the performance of those methods is highly prone to artifacts caused by FPN. We also show that tackling FPN by properly designed suppressing filters leads to considerably better denoising results.

II. TIME-OF-FLIGHT SENSING PRINCIPLE

A ToF range-sensing device has four main modules: a beamer, an electronic light modulator, a sensor chip and a discrete correlator. The light modulator produces a continuously modulated harmonic signal, which is emitted by the beamer. The latter is composed of light-emitting diodes (LED), which operate in the near-infrared wavelength region (~850 nm). The sensor chip is composed of sensing elements forming a discrete matrix offering certain spatial resolution just like other imaging sensors. When the emitted light illuminates the scene objects, the sensor chip senses the reflected signals by collecting charges at the sensing elements during a selected integration time I_T. The phase-delay φ between the emitted and the reflected signals at each pixel depends on the distance to the corresponding area of the scene. It is measured at the discrete correlator for several successive measurements (samples) R_n (n=1,2,…N, N≥4) taken at equal intervals within the same modulated period:

$$A = \frac{2}{N}\sum_{n=0}^{N}\left|R_n e^{-j2\pi\frac{n}{N}}\right|, \varphi = \arg\left(\sum_{n=0}^{N} R_n e^{-j\frac{2\pi n}{N}}\right), \quad (1)$$

where A is the modulation amplitude, and j is the imaginary unit. The sensed distance D is proportional to the phase, while the variance of distance measurements σ_D^2, being measure of their accuracy, is proportional to the square inverse of the amplitude (c.f. Fig. 1):

$$D \propto \frac{\varphi}{4\pi f} c_L, \quad \sigma_D^2 \propto \left(\frac{1}{A^2}\right), \sigma_D^2 \sim \frac{\lambda}{2A^2}, \quad (2)$$

where f is the frequency of the emitted signal, c_L is the speed of light through dry air and λ is tuning parameter [5, 6].

A. Low-sensing environment

While working in normal mode, i.e. when the illumination from the beamer is sufficient, the measured distances are quite precise. Scenes with low reflectance, ambient light, and surfaces causing multi-path reflectance are the general sources of measurement errors. To this end, for the sake of miniaturization and low power consumption, the device might be forced to work in low-sensing mode. This would impose

requirements for limited beamer size, decreased number of LED elements, and shorter integration times. For such mode, the noise becomes a dominant problem, which needs to be tackled properly. The case is illustrated in Figs. 1,2,3.

Fig. 1 plots variances of measured distances σ_D^2 against the measured amplitudes in a Monte Carlo type of measurement experiments. A fitted curve validates Eq. (2). An amplitude threshold can define the low-sensing operating range (e.g. A<300 units). Depth maps sensed in low-amplitude conditions are shown in Fig. 3, for varying integration times I_T= [200,100, 50] μs in comparison to normal operating mode of I_T=2000 μs. The figures illustrate the need of proper denoising procedure to be applied to the calculated distance maps in a post-capture stage – for more details see [5, 6, 7, 8, 9, 10].

B. *Fixed-pattern noise*

Every light-capturing device with digital sensor (*CCD or CMOS*) is influenced by spatially-related offset mask called *Fixed-pattern noise* (*FPN*) [11, 12]. In the case of ToF sensors, FPN appears as stripes of brighter or darker intensity across the image pixels (c.f. Figs 3a,3b, *zoom in PDF file*). The reason of such noise can be explained by the structural non-uniformities of *inputs-outputs* of sensing elements. Those are defined as different operation limits of sensing elements to discharge data of low or oversaturated value charges [5, 11, 12, 13]. Consequently, the noise behavior will be observed in the direction of discharging flow process and it will appear as periodic "*column-*" or "*row-wise*" stripes. Although referred as "*fixed*", the noise behavior changes during exploitation time due to the sensor wearing out. This means that certain easy-to-implement filtering mechanism should exist that could adapt for possible changes in the nature of FPN.

Although visible, for ToF devices, the FPN is not considered important for default operating mode (when A is higher than the low-sensing threshold) [5]. As shown in [5], the influence of such noise is usually below the resolution error, which can be faded further effectively by flat-field correction mechanism. The role of FPN starts to appear important, when the ToF device is used in a low-sensing environment. In such case, the noise levels start to be comparable to the sensed signal, which makes the FPN dominant over the mixture of information signal and spatially-varying noise (c.f. Figs. 3a, 3b). Since FPN creates kind-of a periodic pattern, denoising algorithms consider this pattern as a 'true' signal and amplify its presence thereby diminishing the importance of true (but noisy) data, thus introducing high-error measurement artifacts. The above discussion emphasizes the importance of properly handling such noise for denoising of data recorded in low-sensing environment.

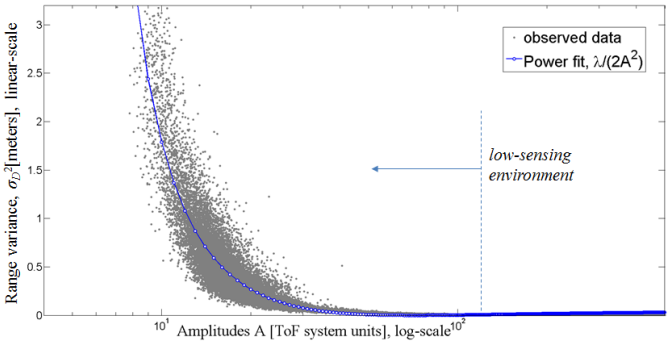

Fig. 1. Empirical dependence between amplitude and variance of distance measuremetns for a ToF device (CamCube 2.0) in low-sensing environment.

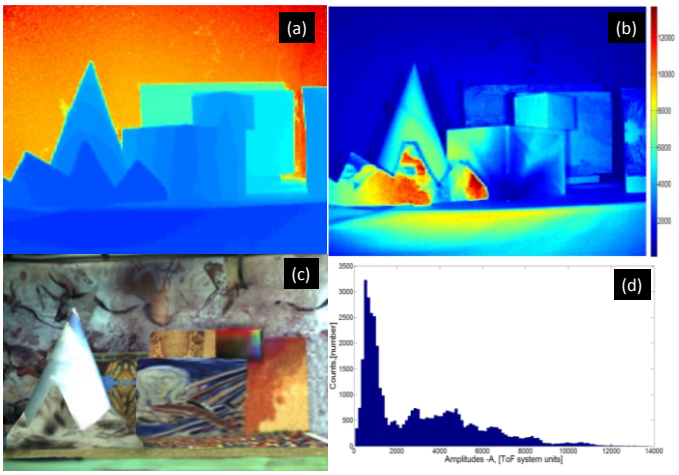

Fig. 2. Modalities in normal sensing mode (CamCube 2.0). (a) Pseudo-color noise-free depth map. (b) Reflectance map (amplitude A). (c) Color scene. (d) Histogram of amplitudes.

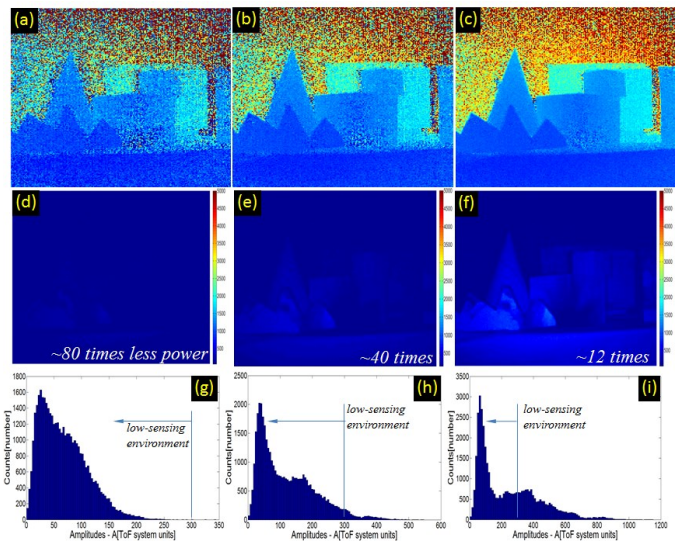

Fig. 3. Depth and aplitude modalities of CamCube 2.0 in low-sensing modes simulated by short integration time I_T, from left to right I_T = 50 μs, 100 μs, 200 μs. Top row: range data maps; mid row: amplitude maps; bottom row: aplitude histograms.

III. DESIGN OF FILTERS FOR REMOVAL OF FPN

As discussed in the previous section, data obtained from a ToF sensor operating in a low-sensing environment is contaminated with two types of noises, namely, spatially-varying noise with Gaussian distribution and FPN. For removing the former, various denoising algorithms can be used (e.g. BM3D [15], NLM [14]) as it will be demonstrated in Section IV. However, in order to obtain good denoising results, before applying a suitable denoising algorithm, the FPN noise has to be removed from the data. In this paper, this is done by means of custom designed notch-type linear-phase finite impulse response (FIR) filters. The design of such filters is described in the rest of this section.

A. Filter specifications

Based on the analysis of sensor data, there are two sets of requirements that a filter for removing the FPN should satisfy. First, as determined by the sensor data (see Fig. 3), the FPN present in the data has two dominant frequencies, namely, $\omega_1 = 2/3\pi$ and $\omega_2 = \pi$. Both of those have to be removed (suppressed). Second, the rest of the data (all other frequencies) should be preserved as well as possible since introduction of variation across frequencies would change the useful content of the data (depth information) and it would modulate the present spatially-varying Gaussian noise, making proper denoising a very difficult (even impossible) task. Following those two sets of requirements, a filter for removal of FPN should satisfy, as illustrated in Fig. 4(a), the following notch-type frequency domain specifications:

$$\left|D(e^{j\omega})\right| = \begin{cases} 1 \text{ for } & \omega \in X \\ 0 \text{ for } & \omega = 2/3\pi, \pi \end{cases} \tag{3}$$

With region X defined as $X = [0, \omega_{p1}] \cup [\omega_{p2}, \omega_{p3}]$

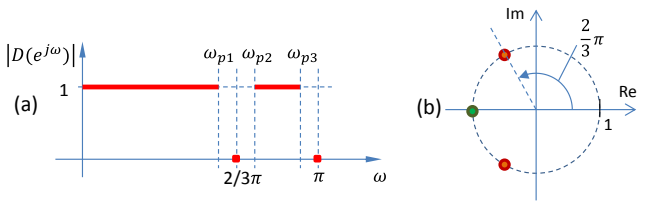

Fig. 4. (a) Desired filter specifications and (b) fixed zeros of filter $H(z)$.

It should be emphasized that in ideal case, the transition bands around $2/3\pi$ and π should be as small as possible, but as it is well known in filter design, from practical perspective they have to be reasonably wide in order to be able to design filters with small passband ripples. Furthermore, for reducing the influence of the filter on the sensor data (e.g. introducing nonlinearity in the phase), we limit ourselves to linear-phase FIR filters. Such filters are relatively easy to design and implement, have a linear phase, and, as it will be seen, can achieve satisfactory performance in the task on hand.

B. Filter design approach

Based on the requirements listed in the previous section, we consider the following design problem: For a given filter order N and region of interest X, determine the unknown filter coefficients $h[n]$ of a linear-phase filter with transfer function $H(z) = \sum_{n=0}^{N} h[n]z^{-n}$ to minimize δ such that

$$1 - \delta \le \left|H(e^{j\omega})\right| \le 1 + \delta \text{ for } \omega \in X$$
$$\left|H(e^{j\omega})\right| = 0 \text{ for } \omega = 2/3\pi, \pi.$$

For solving this problem efficiently, the filter transfer function is first decomposed into three parts as

$$H(z) = A_1(z)A_2(z)G(z) \tag{4}$$

with

$$A_1(z) = 1 + z^{-1} + z^{-2}$$
$$A_2(z) = 1 + z^{-1}$$
$$G(z) = \sum_{n=0}^{N_G} g[n]z^{-n}$$

and $N_G = N - 3$. The functions $A_1(z)$ and $A_2(z)$ are the transfer functions of a zero pair at $\pm 2/3\pi$ (red zeros in Fig. 4(b)) and a zero at π (green zero in Fig. 4(b)), respectively. The corresponding zero-phase frequency responses of those three transfer functions can be expressed as [22], [23]

$$A_1(\omega) = 1 + 2\cos(\omega)$$
$$A_2(\omega) = 2\cos(\omega/2)$$
$$G(\omega) = \begin{cases} g\left[\frac{N_G}{2}\right] + 2\sum_{n=1}^{N_G} g\left[\frac{N_G}{2} - n\right]\cos(n\omega) \text{ for } N_G \text{ even} \\ 2\sum_{n=1}^{N_G} g\left[\frac{N_G - 1}{2} - n\right]\cos\left((n+1)\frac{\omega}{2}\right) \text{ for } N_G \text{ odd} \end{cases} \tag{5}$$

Since $A_1(\omega)$ and $A_2(\omega)$ are fixed, this leaves only the values $g[n]$ for $n = 0,1, \dots, [N_G/2]$ as free variables for optimization. It should be pointed out, that in this design we do not have a classical stopband – that part is taken care by fixed zeros incorporated in the design.

In this paper we use the Remez multiple exchange algorithm for determining the values of $g[n]$ [22, 24]. In the general case, the Remez algorithm can be used for finding filter coefficients of $G(\omega)$ such to minimize

$$\varepsilon = \max_{\omega \in X} |E(\omega)| \tag{6}$$

with

$$E(\omega) = W(\omega)[G(\omega) - D(\omega)],$$

where $W(\omega)$ is the weighting function and $D(\omega)$ is the desired value of the designed filter in the region of interest X. Taking into account the desired values for $H(e^{j\omega})$ as given by (3) and the relation between $H(\omega)$ and $G(\omega)$, in the case under consideration the weighting function and the desired value has to be modified in the design as (see [22] for details)

$$W(\omega) = 1/|A_1(\omega)A_2(\omega)| \tag{7}$$
$$D(\omega) = |A_1(\omega)A_2(\omega)|.$$

The Remez algorithm evaluates the values of $g[n]$ that minimize the error function (6). Based on (5), the filter values $h[n]$ for $n = 0,1, \dots, N$ can be easily obtained by convolving $G(z)$ with $A_1(z)$ and $A_2(z)$.

C. Designed filters

A filter designed with the method proposed in the previous section, has different spatial and frequency domain properties depending on the selected filter order and the passband edges. It is obvious that filters of higher order and wider transition bandwidths have a smaller ripple in passbands, but at the same

time they have higher ringing effects in the spatial domain and remove more of the useful information. Since it is not obvious what the best choice of filter for the removal of FPN for sensors under consideration is, we designed a family of filters having various orders and passband edges. The idea is to test all these filters (see Section IV) on artificial and real sensor data and then select ones that perform best. Moreover, although the passband edges can be freely chosen, we noticed that it is beneficially to choose them such that all transition bandwidths are equal, that is,

$$\begin{aligned} \omega_{p1} &= 2/3\pi - \rho\pi \\ \omega_{p2} &= 2/3\pi + \rho\pi \\ \omega_{p3} &= \pi - \rho\pi \end{aligned} \tag{8}$$

with $\rho \in [0,1/6]$ being a parameter determining the transition bandwidth (values larger than 1/6 result in $\omega_{p2} > \omega_{p3}$ and as such are not practical).

The obtained passband ripples for filters with various filter orders and transition bandwidths, considered in this paper for FPN removal, are shown in Fig. 5. Moreover, as an example, the frequency response of a designed filter ($N = 41, \rho = 0.1$) is given in Fig. 6.

Three comments regarding the designed filters: First, for the same passband performance, a filter with even order must be around 10 orders higher than an odd order filter. The reason for this is in the fact that an even order filter will have, due to its properties [23], two zeros at $\omega = \pi$ instead of one, thereby making the passband optimization more challenging. Second, an odd order filter introduces a half step delay after filtering – this might be a problem when interpreting the depth data. Therefore, also even order filters are considered here although they are not as efficient as odd order ones (passband properties v.r.t. filter order). Third, in the design we assume identical passband ripples in both bands. From the design perspective it is possible to have different ripples in each band – the benefits / drawbacks of that will be studied in future work.

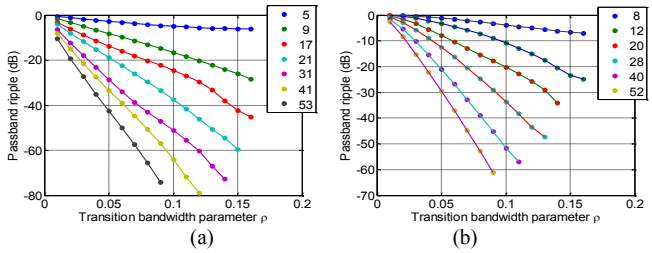

Fig. 5. Performance of designed filters. (a) Odd filter orders. (b) Even filter orders

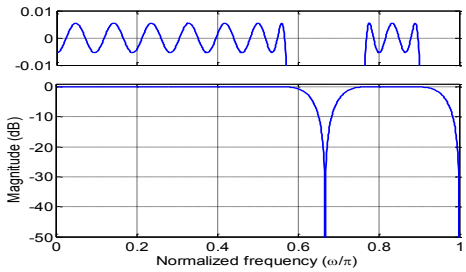

Fig. 6. Magnitude response of a filter with $N = 41$ and $\rho = 0.1$

IV. Experimental results

A. Experimental setup

We apply the proposed filtering solution in two scenarios. In the first scenario, we use a synthetically created scene that is rich in objects of fine details, edges, and contours situated in maximum depth range of typical ToF device $D \in [0, 7.5]$ m. We simulate distance measurement error in low-sensing environment, i.e. for $A \in [0, 300]$ units, following the model in Fig. 1. [5, 6]. This is rather an extreme case, which rarely can happen in reality. However, it is an instructive setting for testing the proposed FPN suppression approach (c.f. Fig. 7). The second scenario considers a real-case experimental setup. It includes a captured scene where the relative object position to camera is kept unchanged, but the sensing conditions are varied by changing the sensor operational parameters (c.f. Fig. 3). Default camera capturing settings and integration time of *2000 μs* has been set to model normal sensing conditions (i.e. amplitude confidence ensuring measuring error smaller than specified for the device). We have prepared Ground Truth (GT) images by averaging 200 consecutively captured frames (c.f. Fig. 2). The testing scene is formed by planar objects facing frontally the camera, and placed at various depth positions. The objects are made from materials of different reflection or painted in different color textures. We model the varying sensing environment by decreasing the integration times for capturing raw samples within the range 50÷200 *μs* (cf. Fig. 3). For each integration time, Table II lists the percentage of pixels which amplitudes A are below the low-sensing threshold (LOW) for this ToF device and pixels with no informative value (IMP) regarded as impulsive noise.

The following denoising methods have been implemented and tested: Non-local Means (NLM) [14], Block matching over 3D (BM3D) [15], sliding DCT (sDCT) [16, 19], cross-bilateral filtering with depth hypothesis (HypBi) [17], and Local polynomial approximation by an intersection of confidence intervals (LPA-ICI) [18, 20]. The denoising performance is made with respect to PSNR calculated according to $D_{MAX} = 7.5$m as follows:

$$MSE = \frac{1}{N_P}\sum_{x=0}^{x<N_P}\left(D_C(x) - D_{GT}(x)\right)^2, PSNR[dB] = 20\log_{10}\left(\frac{D_{MAX}}{MSE}\right) \tag{9}$$

B. Synthetic data experiments

This experiment allows "offline" performance testing of a ToF device working in a low-sensing environment. We test the filters for FPN removal, denoising methods, and optimize adaptive post-filtering stage against particular FPN influence. We demonstrate such "offline" testing scenario for low-sensing environment of PMDTech CamCube 2.0 camera [2] and apply expected FPN [5, 6] for ω_{FPN} = [1, 2/3]×π with intensity corresponding to the sensed amplitude A:

$$D_{FPN} = D + D\cos(\omega_{FPN})(\alpha A^{\beta} + \gamma), \tag{10}$$

where α = –3.966, β=0.012, γ=5.25. This ensures that the added FPN is 25% of the signal value for very low-sensed signals and less than 5% for signals above the low-sensing environment. Since the FPN is more dominant for very low-

sensed signals, the filtering process can be adapted in a manner that filtered output D_F and original data input D_{FPN} are fused in certain normalized fraction (δ_A, $1-\delta_A$) according to signal amplitudes A:

$$D_{ADA} = \delta_A D_F + (1-\delta_A) D_{FPN} \,. \tag{11}$$

This helps in preserving data edges. For very low amplitudes ($A \le 70$), $\delta_A = 1$, while for the range of amplitudes [70, 350], it decreases linearly between 1 and 0.2. In Fig. 9 we provide results for proposed filters depicted in Fig. 5. We also give results for few of them in Table I. From Fig. 8 and Table I we demonstrate that FPN can be effectively suppressed, resulting in a 5-6 dB improvement of the denoising performance (e.g. NLM method).

TABLE I. FPN FILTERING PERFORMANCE ON SYNTHETIC DATA

{order, ρ}	**Denoised results for NLM method[14]** (not filtered, *filtered*, ***+adaptive***)**[dB]**	
	with FPN(24.51dB)	*noise added(21.26dB)*
Input[dB]	(25.28, -, -)	(24.79,-, -)
{20, *0.14*}	(25.28, *30.20*, **31.45**)	(24.79, *29.51*, **30.58**)
{28, *0.13*}	(25.28, *30.32*, **31.33**)	(24.79, *29.56*, **30.48**)
{40, *0.09*}	(25.28, *30.04*, **31.10**)	(24.79. *29.28*, **30.24**)
{17, *0.14*}	(25.28, *28.35*, **30.44**)	(24.79, *27.80*, **29.62**)
{31, *0.14*}	(25.28, *28.29*, **30.43**)	(24.79, *27.74*, **29.60**)
{41, *0.12*}	(25.28, *28.18*, **30.26**)	(24.79, *27.62*, **29.48**)

TABLE II. DENOISING RESULTS FOR REAL-CASE DATA

Method	(not filtered, ***filtered***) **for FPN[dB]**		
	I_T=50μs	***I_T=100μs***	***I_T=200μs***
{LOW,IMP}[%]	*{100, 11}*	*{94, 5}*	*{83, 2}*
No denoising	(19.3, ***21.3***)	(22.3, ***24.3***)	(26.3, ***27.6***)
NLM[14]	(22.1, ***26.7***)	(27.3, ***30.4***)	(32.8, ***35***)
HypBi[17]	(20.8, ***25***)	(23.6, ***28.4***)	(28.7, ***32.4***)
LPA-ICI[18]	(24.6, ***28.8***)	(28.9, ***31.8***)	(33.8, ***35.1***)
BM3D[15]	(24.3, ***28.4***)	(28.8, ***31.4***)	(32.9, ***35.4***)
sDCT[16]	(24.4, ***26.4***)	(26.2, ***27.9***)	(27.8, ***28.1***)

C. *Real-case data experiment*

The real case experiment supports evidence that denoising of low-sensing environment benefits from the proposed filtering solution. As seen in Table II, for extreme measurement error (e.g. I_T=50μs), the denoising performance is always 3-5 dB better with respect to the case when FPN is not properly addressed. The visual plots in Figs. 10, 11 reveal the performance boost by apparent sensing improvement and artifacts suppression. Obviously, the role of FPN starts to fade when sensed signal becomes stronger (e.g. I_T=200μs).

V. CONCLUDING REMARKS

By means of examples, we have shown the importance of removing the FPN from the measured data before a denoising algorithm is used. For the purpose of removing the FPN, we applied several filters designed with the proposed approach and compared their performance in terms of PSNR. Several good candidates have been identified that performed very well on both, the synthetic and real data. This indicates that additional constraints could be added to the FPN filter design that potentially could further improve the measured depth.

Finally, it is worth mentioning that although in this paper we illustrated the approach on one off-the-shelf ToF sensor, similar FPN appears in all ToF devices and as such the proposed approach can be used, with small adaptations, with any similar device.

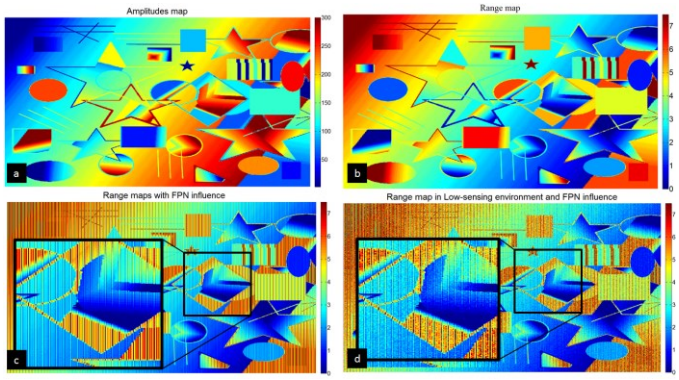

Fig. 7. Synthetic scene for low-sensing ToF sensing environment: (a) GT amplitude map, (b) GT range map, (c) FPN influence on measured depth (d) noise contamination; (zoomed region in black squares)

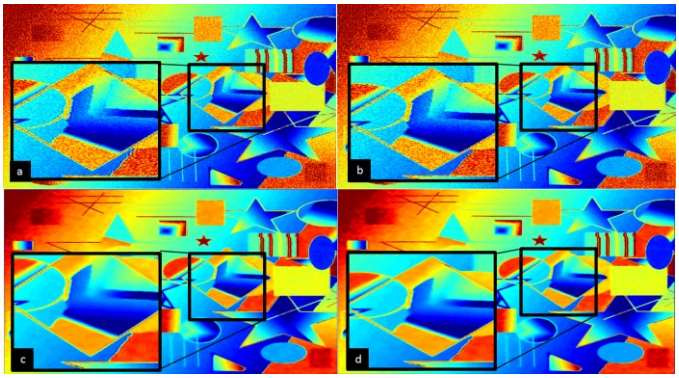

Fig. 8. FPN suppression using filter {20, 0.14} for the synthetic scene experiment: (a) filtered and (b) adapted filtering output, and their corresponding subsequently denoised versions (c), (d)

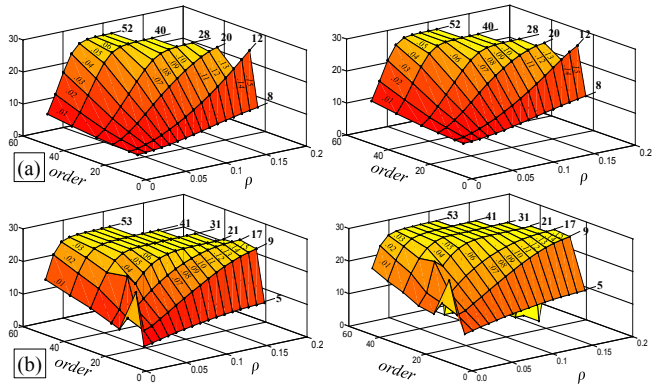

Fig. 9. Performance (PSNR) of NLM denoising method after suppression of FPN with filters of even order (first row) and odd order (second row) with adaptation (second column) and without adaptation (first column).

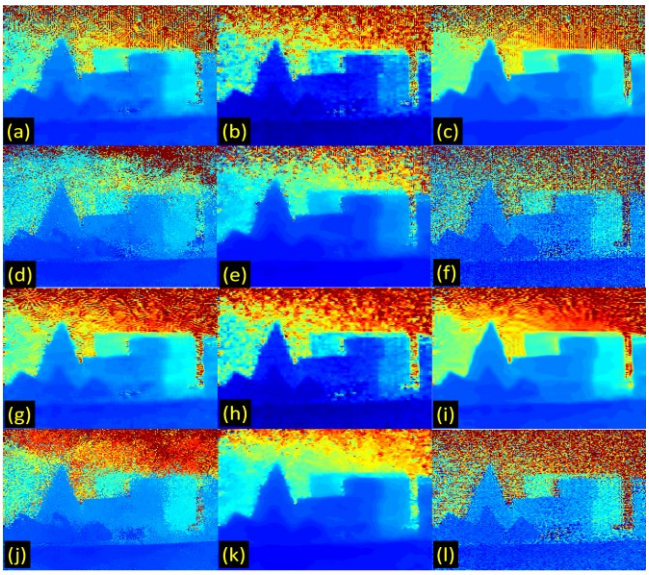

Fig. 10. Performance of denoising methods for real-case scene data with respect to FPN suppression and for methods: (a) NLM, (b) sDCT, (c) BM3D, (d) HypBi, (e) LPA-ICI for (f) noisy input I_T = 50μs; and (g)–(l) corresponding outputs after FPN adaptive filtering

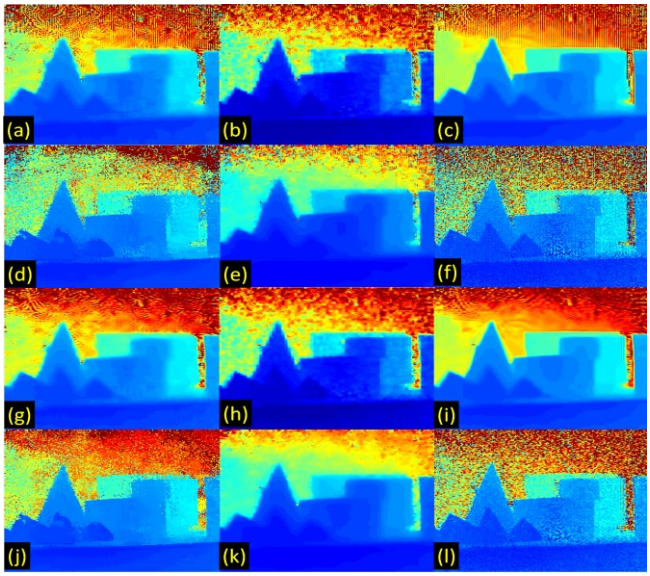

Fig. 11. Performance of denoising methods for real-case scene data wrt FPN suppression: (a) NLM, (b) sDCT, (c) BM3D, (d) HypBi, (e) LPA-ICI for (f) noisy input I_T = 100μs; and (g)–(l) corresponding outputs after FPN adaptive filtering

REFERENCES

[1] Microsoft, Canesta, "Kinect 2.0 – Build natural interface apps," ToF camera vendor, info@microsoft.com, Seattle, USA 2013.

[2] PMDTechnologies GmbH, "PMD[Vision] CamCube 2.0," *PMD Camera Vendor*, info@pmdtec.com, Siegen, Germany, 2010.

[3] R. Lange, P. Seitz, "Solid-state time-of-flight range camera", *IEEE Journal of Quantum Electronics,* vol. 37 (3), pp. 390-397, March 2001.

[4] T. Ringbeck, B. Hagebeuker, "A 3D time of flight camera for object detection," *Proc of Optical 3D Measurement Techniques*, Zurich, Switzerland, 10 pages, Setp. 2007.

[5] H. Rapp, "Experimental and theoretical investigation of correlating ToF-camera systems," PhD Thesis, University of Heidelberg, Germany, 2007.

[6] M. Frank, M. Plaue, H. Rapp, U. Koethe, B, Jähne, F. A. Hamprecht. "Theoretical and experimental error analysis of continuous-wave time-of-flight range cameras," *Optical Engineering*, vol. 48(1), 16 pages, Jan. 2009.

[7] M. Georgiev, A. Gotchev, M. Hannuksela, "De-noising of distance maps sensed by time-of-flight devices in poor sensing environment," *Proc. IEEE Conf. on Acoustics Speech and Signal Processing (ICASSP)*, pp. 1533-1537, Vancouver, Canada, May 2013.

[8] M. Georgiev, A. Gotchev, M. Hannuksela, "Joint de-noising and fusion of 2D video and depth map sequences sensed by low-powered tof range sensor," *Proc. of IEEE Conf. on Multimadeia and Expo Workshops (ICMEW)*, San Jose, California, 4 pages, July, 2013.

[9] M. Georgiev, A. Gotchev, M. Hannuksela, "Real-time denoising of ToF measurements by spatio-temporal non-local mean filtering," *Proc. of IEEE Conf. on Multimadeia and Expo Workshops (ICMEW)*, San Jose, California; 6 pages, July, 2013.

[10] A. Chuchvara, M. Georgiev, A. Gotchev, "A speed-optimized RGB-Z capture system with improved denoising capabilities," *Proc. of SPIE, Image Processing: Algorithms and Systems XII*, vol. 9019, 13 pages, March. 2014.

[11] A. Foi, M. Trimeche, V. Katkovnik, "Practical poissonian-gaussian noise modeling and fitting for single-image raw-data," *IEEE Trans. on Image Processing*, vol. 17(10), pp. 1737-1754, Oct. 2008.

[12] M. Maggioni, E. S. Monge, A. Foi, "Joint removal of random and fixed-pattern noise through spatiotemporal video filtering," *IEEE Trans. Image Processing*, vol. 23(10), pp. 4282-4296, Oct. 2014.

[13] J. E. Pezoa, O. J. Medina, "Spectral model for fixed-pattern-noise in infrared focal-plane arrays," *Progress in Pattern Recognition, Image Analysis, Computer Vision, and Applications - LNCS* vol. 7042, pp. 55-63, Nov. 2011.

[14] A. Buades, B. Coll, J. Morel, "A non-local algorithm for image denoising," *Proc. of IEEE Conf. on Computer Vision and Pattern Recognition (CVPR)*, vol. 2, pp. 60-65, San Diego, California, June, 2005

[15] K. Dabov, A. Foi, V. Katkovnik, K, Egiazarian, "Image denoising by sparse 3-D transform-domain collaborative filtering," *IEEE Trans. on Image Processing*, vol. 16(8), pp. 2080-2095, Aug. 2007.

[16] R. Öktem, L. Yaroslavsky, K. Egiazarian, "Signal and image denoising in transform domain and wavelet shrinkage: A comparative study," *Proc. of European Signal Process. Conf (EUSIPCO)*, vol.9, pp. 2269-2272, Rhodes, Greece, Sept. 1998.

[17] S. Smirnov, A. Gotchev, K. Egiazarian, "Methods for depth-map filtering in view-plus-depth 3D video representation," *EURASIP Journal on Advances in Signal Processing*, vol. 15(2), 21 pages, Feb. 2012.

[18] V. Katkovnik, A. Foi, K. Egiazarian, J. Astola, "Directional varying scale approximations for anisotropic signal processing," Proc. of XII *European Signal Process. Conf. (EUSIPCO)* vol. 1, pp. 101-104, Sept, 2004.

[19] A. Shulev, A. Gotchev, "A sliding-window transform-domain technique for denoising of DSPI phase maps," *Proc. of SPIE, Image Processing: Algorithms and Systems XII*, vol. 90190N, March. 2014.

[20] V. Katkovnik, J. Astola, K. Egiazarian, "Phase local approximation (phasela) technique for phase unwrap from noisy data," *IEEE Trans. on Image Processing* vol. 17 (6) pp. 833-846, June 2008.

[21] V. Katkovnik, J. Bioucas-Dias, N. Petrov, "Digital phase-shifting holography based on sparse approximation of phase and amplitude," *Proc. 3DTV-Conference*, 4 pages, Budapest, Hungary, June 2014.

[22] T. Saramäki, "Finite impulse response filter design", Chapter 4 in *Handbook for Digital Signal Processing* edited by S. K. Mitra and J. F. Kaiser. John Willey & Sons, New York, 1993.

[23] S. K. Mitra, *Digital Signal Processing: A Computer-Based Approach,* McGraw-Hill, New York, 2006.

J. H. McClellan, T. W. Parks, and L. R. Rabiner, "A computer program for designing optimum FIR linear phase digital filters," *IEEE Trans. on Audio Electroacoustics*, vol. AU-21, pp. 506-526, Dec. 1973.